

## Supplementary Information

### Photothermally Powered Conductive Films for Absorber-Free Solar Thermoelectric Harvesting

Byeongwan Kim, Minsu Han, and Eunyoung Kim\*

Department of Chemical and Biomolecular Engineering, Yonsei University, 50 Yonsei-ro,  
Seodaemun-gu, Seoul 03722, South Korea

---

<b>Section 1. Experimental details</b> .....	<b>S3</b>
<b>Section 2. Supplementary tables</b> .....	<b>S12</b>
Table S1. Preparation of PEDOT films with different conductivities and their electronic properties.	
Table S2. The peak assignment and degree of crystallinity of various PEDOT films.	
Table S3. Film geometry and properties for simulation.	
Table S4. The parameters for calculation of the photothermal conversion efficiency.	
Table S5. Comparison of the NIR sensitivities of photothermal photodetectors from the literature.	
Table S6. Photothermoelectric voltage and power generation under solar light with various thickness samples.	
Table S7. Comparison of the solar thermoelectric performance from the literature.	
<b>Section 3. Supplementary Figures</b> .....	<b>S22</b>
Figure S1. UV-vis-NIR spectrum.	
Figure S2. Two-dimensional GIWAXS patterns for different PEDOT films.	
Figure S3. Two-dimensional GIWAXS patterns for a P4 film with different X-ray beam directions in $x$ - $y$ plane	

Figure S4. DLS analysis.

Figure S5. Thermal images.

Figure S6. Photothermal conversion efficiency of PEDOT with various polymerization conditions as a function of maximum temperature increase using 808 -nm and 1064 -nm lasers.

Figure S7. The photothermal conversion efficiency as a function of Hall carrier mobility.

Figure S8. Photothermal simulation.

Figure S9. Seebeck voltage and current generation of PEDOT films with various conductivities.

Figure S10. PTE voltage and current generation with different electrode distances under 808 -nm laser irradiation (153 mW) of 180 -nm-thick P4 films on PET under ambient conditions.

Figure S11. The changes in the photo-Seebeck coefficients per unit absorbed light power.

Figure S12. The correlation of the photothermoelectric power output and degree of crystallinity in PEDOT films.

Figure S13. Photothermoelectric device system under solar light

Figure S14. Photothermoelectric voltage and temperature generation under solar light.

**Section 4. Supplementary references ..... S36**

## Section 1. Experimental details

### Materials

Iron(III) *p*-toluenesulfonic acid monohydrate, iron(III) *p*-toluenesulfonate hexahydrate, poly(ethylene glycol)-block-poly(propylene glycol)-block-poly(ethylene glycol) (PEPG, average molecular weight 2800), 3,4-ethylenedioxythiophene (EDOT), pyridine, ferrocene, anhydrous *n*-butanol, isopropyl alcohol, tetrabutylammonium perchlorate, and anhydrous propylene carbonate were purchased from Aldrich Chemicals. Other materials were used without further purification.

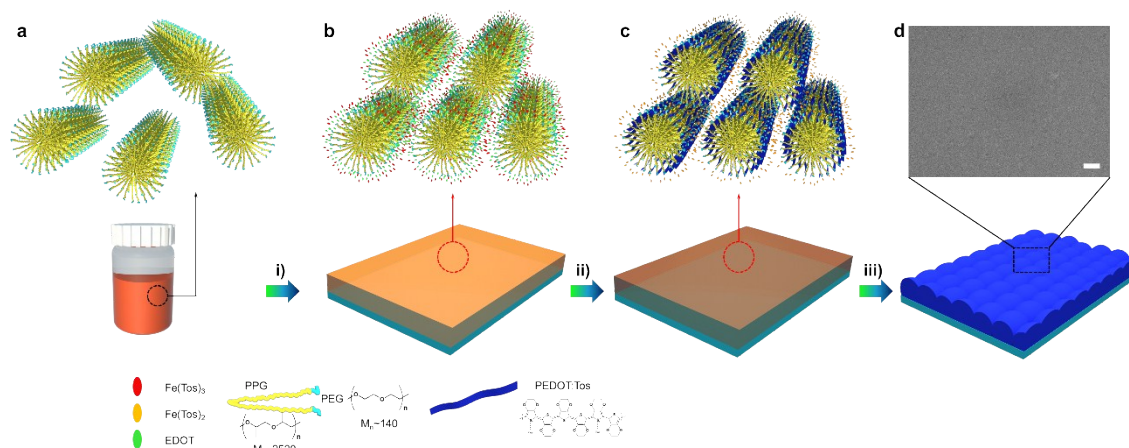
### Methods

#### Synthesis of iron(III) *p*-toluenesulfonate

Iron(III) *p*-toluenesulfonate was synthesized from iron(III) chloride hexahydrate ( $\text{FeCl}_3 \cdot 6\text{H}_2\text{O}$ ) in 2 steps as previously reported. Iron(III) chloride hexahydrate (10.0 g) was mixed and reacted with excess NaOH (4.93 g) in an aqueous solution for 1 h at room temperature. The brown precipitate was filtered, washed two times with distilled water, and dried at 40 °C for 12 h in a vacuum oven. The obtained powder (3.8 g) and *p*-toluenesulfonic acid monohydrate (23.5 g) were mixed in methanol (70 mL) at 45 °C for 3 h. After the brown powder dissolved in solution, the solvent was evaporated, and an orange powder was obtained after drying in a vacuum oven at 70 °C. The solid product was stored in a desiccator.

#### Preparation of the P4 films

P4 films were prepared using solution casting polymerization (SCP). PEPG (0.20 g) was added to the oxidative solution (1.0 g, 40 wt% of iron(III) *p*-toluenesulfonate in *n*-butanol) and stirred for 2 h. Pyridine (11.6 mg) was added to the solution and stirred for 2 h. Then, a homogeneous red solution was obtained by filtration using a hydrophilic syringe filter (0.45  $\mu\text{m}$ ) and EDOT (37.8 mg) was added prior to use. The molar composition of the mixture was monomer:iron(III) *p*-toluenesulfonate:pyridine=1:2.64:0.55. Large PET films or glass slides (2.5×3 to 5×7 cm<sup>2</sup>) were treated with O<sub>2</sub> plasma for 3 min with a flow rate of 40.0 sccm to increase the uniformity of the polymer film. The monomeric solution was spin coated onto the substrates using various spin speeds (700–2500 rpm) to control the thickness of the final polymer films and heated at 60–80 °C and 35% RH for 2 h as shown in Table S1. Then, the polymer films were washed with ethanol to remove the catalyst, residual oxidant, and impurities. Finally, the polymer films were dried under N<sub>2</sub> flow and annealed at 60 °C for 5 min. Polymerization mechanism is shown in Scheme S1.



**Scheme S1. Schematic presentation of the synthesis of highly crystalline PEDOT:Tos film.** (a) PEPG in *n*-butanol solution. (b) Spin-coated mixture solution on the substrate. (c) Polymerized PEDOT:Tos in the composite. (d) Highly crystalline PEDOT:Tos film. A SEM image of P4. Scale bar: 1  $\mu\text{m}$ . i) Spin-coating process; ii) 60  $^{\circ}\text{C}$  for 10 min; and iii) washing with ethanol for two times.

### Preparation of the P2 films

The P2 films were prepared using different spin coating speeds, as shown in Table S1. PEPG (0.2 g) was added to the oxidative solution (1.0 g, 40 wt% of iron(III) *p*-toluenesulfonate in *n*-butanol) and stirred for 2 h. Pyridine (13.5 mg) was added into the solution and stirred for 2 h. Then, a homogeneous red solution was obtained by filtration using a hydrophilic syringe filter (0.45  $\mu\text{m}$ ) and EDOT (44.1 mg) was added prior to use. Further steps were performed the same as previously described.

### Preparation of the P7–9 films

The P7–9 films were prepared using the SCP solution compositions shown in Table S1. Specific amounts of PEPG were added into the oxidative solutions (1.0 g, 20 wt% of iron(III) chloride in *n*-butanol) and stirred for 2 h. Then, a homogeneous red solution was obtained by filtration using a hydrophilic syringe filter (0.45  $\mu\text{m}$ ) and EDOT (65 mg) was added prior to use. Further steps were performed the same as previously described.

### Preparation of the P10–11 films

The P10–11 films were prepared using the SCP solution compositions shown in Table S1. Distilled water (0.3 g) and specific amounts of pyridine were added into the oxidative solutions (0.7 g, 36 wt% of iron(III) *p*-toluenesulfonate in isopropyl alcohol) and stirred for 30 min. Then, a homogeneous red solution was obtained by filtration using a hydrophilic syringe filter (0.45  $\mu\text{m}$ ) and specific amounts of EDOT was added prior to use. Further steps were performed the same as previously described.

### **Measurement of the optical and photothermal properties**

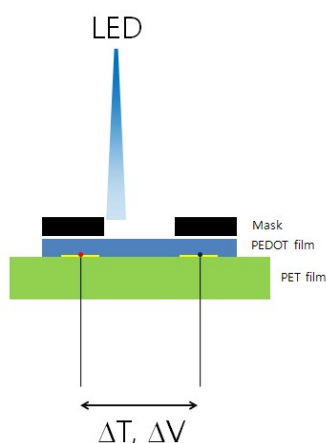
The electrochemically controlled polymer films were prepared using a constant potential method by applying a constant setting potential vs. Ag/AgCl, and the optical and photothermal properties were measured using these films. UV-vis-NIR spectra (Lambda 750, UV/Vis/NIR Spectrophotometer, PerkinElmer) were measured as a function of the applied potential. The NIR coherent diode laser (808 nm, 0–220 mW, B&W Tek, Inc.) emitted perpendicularly to the films (15 cm apart), and the laser beam was collimated to generate a beam size of 3 mm and beam area of 7 mm<sup>2</sup>. The temperature gradients and time-drive temperature changes in the conductive polymer films due to the photothermal effect were measured using a high-resolution IR camera (Testo 875-1 or FLIR E40) and control programmed software in a dark room at room temperature, which was set to 23–25 °C with an error of 0.2 °C, for clear analysis. The photothermal effect experiments were difficult to perform in the chamber (volume of 7500 cm<sup>3</sup>) because the internal temperature increased due to the high local photothermal conversion.

### **Measurement of thermoelectric and photothermoelectric properties**

The Seebeck voltage and the temperature gradient were measured using a homemade shielded setup and an Agilent 34410A Multimeter and Agilent 34970A, respectively. The parallel Au electrodes were thermally evaporated at a rate of 1 Å s<sup>-1</sup> on a polymer film with a size of 2×0.2 cm<sup>2</sup> and a thickness of 100 nm at a pressure of 5×10<sup>-6</sup> mbar using a stainless steel shadow mask.<sup>[1]</sup> The doping level of the film was precisely controlled by cyclic voltammetry, and the cyclic voltammogram was stopped at the desired potential in the conductive electrode-free polymer film used as a self-electrode. In general, two Peltier devices were fixed on an aluminum heat sink using thermal paste (PK-3, Prolimatech), and a temperature gradient was generated between the two Peltier devices (~4 mm gap) (Scheme S2). The temperature gradient was controlled using a Keithley 2400 Multimeter by changing the input current to the two Peltier devices simultaneously. The temperature gradient between the two Peltier devices was measured using T-type thermocouples, which were placed in contact with the two Au electrodes using a z-direction controllable stage. Eleven points for ΔT and ΔV were obtained 3 times by changing the source current for each sample and linearly plotted to calculate the Seebeck coefficient. All of the thermoelectric measurements were performed at room temperature. For the temperature dependent experiment, probe station (Probe station, M5VCMF, MS Tech, Inc.) was used same setting above

The photothermoelectrically generated temperature gradients, voltages, and currents were measured using a similar procedure to that for the thermoelectric properties. A polymer film on the PET film was laminated using a thermal coater. The temperature gradient was controlled by the intensity of the NIR laser, which was irradiated on one side of the polymer film from 2.33 to 0 W cm<sup>-2</sup> in the probe station at 30 mTorr or at atmospheric pressure (~760 Torr). An LED was controlled by the current from the source meter and irradiated on one side of the films with a diameter of 3 mm. The colors of the LED lights were ultraviolet, blue, green, and red and had maximum intensity peaks of 400, 460, 532, and 630

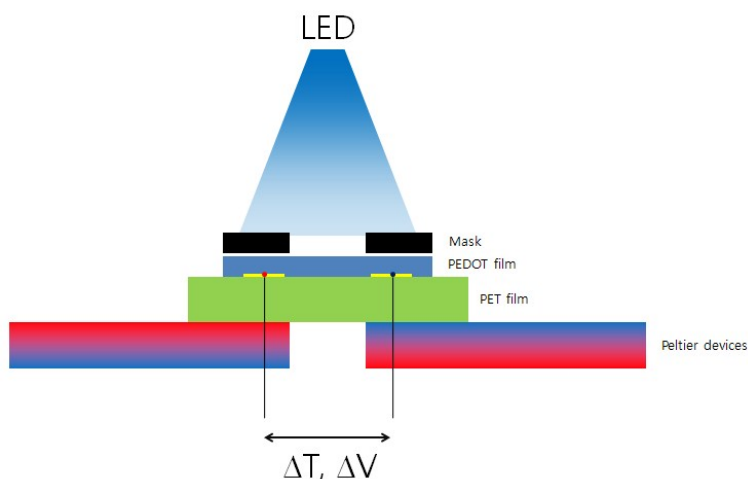
nm, respectively. Five points for  $\Delta T$ ,  $\Delta V$ , and resistance were obtained 3 times by changing the source current for each sample and linearly plotted to calculate the photothermal voltage. All of the photothermoelectric measurements were performed at room temperature. A halogen lamp source was controlled using a fiber source measurement system and irradiated on one side of the films with a diameter of 2 mm. The generated voltages or currents were measured using a Keithley 2636 SYSTEM SourceMeter and TRX-50-1 triaxial cable (Trompeter electronics).



**Scheme S2.** Measurement settings for the photothermoelectric effect

### Measurement of photo-Seebeck properties

The photo-Seebeck voltage was measured using a similar procedure to that for the thermoelectric properties (Scheme S3). The polymer and an Au electrode were laminated on the PET film using a thermal coater. An LED light source was controlled by the current from the source meter, and the colors of the LED lights were blue and red, which had maximum intensity peaks at 460 and 630 nm, respectively. The thermocouples and electrodes were covered with a stainless steel plate to prevent the photovoltaic effect, and the illuminated area was 10 cm<sup>2</sup>. The electrical resistivity was measured using the two-wire method. The temperature gradient was controlled using a Keithley 2400 Multimeter by changing the input current to the two Peltier devices simultaneously. The temperature gradient between the two Peltier devices (4 mm) was measured using T-type thermocouples, which were placed into contact with the two Au electrodes using a z-direction controllable stage. Eleven points for  $\Delta T$ ,  $\Delta V$ , and resistance were obtained 10 times by changing the source current for each sample with three different temperature gradients and linearly plotting to calculate the Seebeck coefficient. All of the photo-Seebeck measurements were performed at room temperature.



**Scheme S3.** Measurement settings for the photo-Seebeck effect

### Measurement of the photothermoelectric devices.

The photothermoelectric voltage and current were measured using a Keithley 2182A Nanovoltmeter and 6485 Picoammeter, respectively, and the source-drain and gate voltages were controlled using a Keithley 2636 System Sourcemeeter. An Al gate electrode (1 mm width and 100 nm thickness) was thermally evaporated on the polyimide film at a pressure of  $5 \times 10^{-6}$  mbar and a rate of  $1 \text{ \AA s}^{-1}$  using a stainless steel shadow mask. Then, a 7 wt% polymethyl methacrylate (PMMA) acetonitrile solution was spin coated on the above film at 2,000 rpm for 30 s to obtain a 500 nm-thick dielectric film. The parallel source-drain Au electrodes were thermally evaporated on the polymer film at a size of  $5.25 \times 0.2 \text{ mm}^2$  and a thickness of 100 nm as well as a pressure of  $5 \times 10^{-6}$  mbar and a rate of  $1 \text{ \AA s}^{-1}$  using a stainless steel shadow mask. Various polymer films were spin coated on the previous films to fabricate transistor-type photothermoelectric devices. The photothermoelectric voltages and currents were detected at 808 nm for the NIR photodetector at room temperature in a 3-mTorr vacuum chamber (Probe station, M5VCMF, MS Tech, Inc.). The laser diameter was 38  $\mu\text{m}$ . The NIR on/off switching was controlled by a shutter (UNIBLITZ, UMM-T1), and the photothermoelectric switching signal was obtained using a Tektronix DPO4104B digital phosphor oscilloscope. A solar simulator (1,000 W Xenon lamp, Oriel, 91193) was used for photothermoelectric properties of polymer films under One Sun. The light intensity was homogeneous across a 8 inch $\times$ 8 inch area and was calibrated with a Si solar cell (Fraunhofer Institute for Solar Energy Systems, Mono-Si+ KG filter, Certificate No. C-ISE269) to a sunlight intensity of  $100 \text{ mW cm}^{-2}$ . This calibration was confirmed with a NREL-calibrated Si solar cell (PV Measurements Inc.). The size and focal length of Fresnel lens (32-683, Edmond Optics) were 5.0 inch $\times$ 5.0 inch and 2.8 inch. The samples were irradiated by the light in the area having  $\sim 200 \text{ mW cm}^{-2}$  light intensity by placing the samples at  $\sim 2$  cm apart from the focused light source. A distance between the sample and Fresnel lens was 7 cm. The measured temperature range of  $S_{\text{PTE}}$  was 25–80  $^{\circ}\text{C}$ .

### Calculation of the photothermal conversion efficiency in the film state

The photothermal conversion efficiency of the polymer films was calculated by modifying the previous report on the solution state by Roper *et al.*<sup>[2]</sup> Detailed equations are given below.<sup>[3, 4]</sup> The total energy balance of the system comprising a substrate and a polymer film under irradiation by an NIR laser is:

$$\sum_i m_i C_{p,i} \frac{dT}{dt} = \sum_j Q_j = Q_{PT} + Q_{sub} - Q_{surr} \quad (S1)$$

where  $m_i$ ,  $C_{p,i}$ ,  $T$ , and  $t$  are the mass of the system components, the heat capacity of system components (PET:  $3.7486 \times 10^{-3} T + 0.04359 \text{ J g}^{-1}\text{K}^{-1}$ , glass slide:  $6.906 \times 10^{-4} T + 0.629 \text{ J g}^{-1}\text{K}^{-1}$ , PEDOT:  $1.73 \text{ J g}^{-1}\text{K}^{-1}$ ), the temperature, and the time, respectively.  $Q_{PT}$  is the photothermal heat energy induced from NIR laser irradiation of the polymer film that generates heat through electron-phonon relaxation, presented as Equation S2:

$$Q_{PT} = I_0 (1 - 10^{-A_\lambda}) \eta_{PT} \quad (S2)$$

where  $I_0$ ,  $A_\lambda$ , and  $\eta_{PT}$  are the laser power, absorbance at the laser wavelength, and photothermal conversion efficiency.  $Q_{sub}$  is the heat dissipated from light absorbed by the substrate without the sample film.  $Q_{surr}$  is the outgoing thermal energy through heat convection, conduction, radiation, etc.  $Q_{surr}$  is linearly increased with temperature for the outgoing thermal energy:

$$Q_{surr} = ha(T - T_{surr}) \quad (S3)$$

where  $h$  is the heat-transfer coefficient,  $a$  is the surface area of the film, and  $T_{surr}$  is the ambient temperature of the surroundings. The temperature at PEDOT film reaches the maximum (equilibrium state) when the heat input is equal to the output:

$$Q_{PT} + Q_{sub} = Q_{surr-max} = ha(T_{max} - T_{surr}) \quad (S4)$$

where the  $Q_{surr-max}$  is the heat flow away from the film surface through air when the film reaches the equilibrium temperature and  $T_{max}$  is the maximum equilibrium temperature of the film. The photothermal conversion efficiency ( $\eta_{PT}$ ) can be determined by substituting Equation S2 for  $Q_{PT}$  into Equation S4 and rearranging to obtain:

$$\eta_{PT} = \frac{ha(T_{max} - T_{surr}) - Q_{sub}}{I_0 (1 - 10^{-A_\lambda})} \quad (S5)$$

where  $Q_{sub}$  was measured independently using a pure PET film without a PEDOT layer. However, the temperature change by the NIR laser is almost undetectable (<1 K) and the power change was <0.5 mW for both 808-nm (power: 0.19 W) and 1064-nm (0.22 W) laser irradiation.  $T_{surr}$  was 24 °C according to Figure S5. The absorbance of the films at 808 nm and 1064 nm are summarized in Table S4 (Figure 1 and Figure S1). The  $ha$  was obtained from the cooling part of the graph (Figure 2b and Figure S5g) using a dimensionless temperature ratio term,  $\theta$  (Equation S6), and time constant,  $\tau_s$  (Equation S7).

$$\theta = \frac{T - T_{surr}}{T_{max} - T_{surr}} \quad (S6)$$

$$\tau_s = \frac{\sum_i m_i C_{p,i}}{ha} \quad (S7)$$

$\theta$  is the driving force temperature and  $\tau_s$  expresses natural heat loss over time during the cooling process in the dark. Equation S7 can be substituted into Equation S1 and rearranged to give:

$$\frac{d\theta}{dt} = \frac{1}{\tau_s} \left[ \frac{Q_{PT} + Q_{sub}}{ha(T_{max} - T_{surr})} - \theta \right] \quad (S8)$$

During the cooling process, when the laser was shut off, the sum of  $Q_{PT}$  and  $Q_{sub}$  become zero, giving:

$$dt = -\tau_s \frac{d\theta}{\theta} \quad (S9)$$

The integration of Equation S9 affords a linear relationship between  $t$  and  $\ln \theta$  with a slope of  $\tau_s$ .

$$t = -\tau_s \ln \theta \quad (S10)$$

Using Equation S7, which was rearranged to Equation S11,  $ha$  was determined as summarized in Table S4.

$$ha = \frac{\sum_i m_i C_{p,i}}{\tau_s} \quad (S11)$$

In this way, we determined for every sample as summarized in Table S4.

### Carrier concentration and mobility were analyzed as below:

In degenerate semiconductive polymers or semimetallic conductive polymers, the oxidation level is important because it directly affects the carrier concentration ( $p$ ) of the materials. Increases in the oxidation level cause increased conductivity because of the higher  $p$  in the valence ( $p$ -type material) or conduction ( $n$ -type material) bands of the materials. With PEDOT, holes are the majority carriers and electrons are the minority carriers, making it a  $p$ -type conductive polymer. Through the Hall effect measurement, the  $p$  and carrier mobility ( $\mu$ ) were obtained with films of different thicknesses.

To demonstrate the electronic states, the  $p$  of various PEDOT films with varied conductivities were explored. According to the Fermi–Dirac distribution function ( $f(E)$ ) and the function of the density of states (DOSs,  $g_v(E)$ ) for  $p$ -type materials, the  $p$  of the degenerate semiconductor can be calculated by integrating the function of DOSs with the probability density function over all possible states:<sup>[5]</sup>

$$p =$$

$$p = \int_{-\infty}^{E_V} g_V(E)\{1 - f(E)\}dE = \frac{4\pi}{h^3}(2m^*)^{\frac{3}{2}} \times \int_{-\infty}^{E_V} \frac{(E_V - E)^{\frac{1}{2}}}{1 + e^{\frac{E_F - E}{kT}}} dE \quad (\text{S12})$$

where  $E_V$  is the top of the valence band. In the case of  $E_V = E_F$ , the integral term of Equation S12 is calculated as a constant of 0.6781. Therefore, in that case, the calculated  $p$  is  $3.0 \times 10^{21} \text{ cm}^{-3}$  for a 180-nm-thick polymer film. This calculated value is similar to the measured value.

#### Measurement of reflectance and calculation of emissivity for P4.

Reflectance spectra for P4 was obtained from the universal reflectance accessory (60 mm PMT/PbS Integrating Sphere) of Lambda 750, UV/Vis/NIR Spectrophotometer, PerkinElmer. The PT temperature distribution of P4 on PET film was simulated using the model for heat transfer in a solid by COMSOL Multiphysics® software (Table S3 and Fig. S8). A three-dimensional modeling of the samples under 808-nm NIR irradiation was performed using the same experimental conditions. Heat transfer by conduction through two layers was selected as the natural cooling system. Convective and radiative heat transfer through the surrounding system (air) was assumed as constant. The boundary condition was room temperature. Simulation parameters are as shown in Table S3. The simulation result was similar to the previous result within ~0.5 K difference.<sup>[6]</sup>

In the thermal radiation, the emissivity at room temperature ( $\varepsilon$ ) can be determined by averaging the spectral data over target wavelength region of a blackbody at room temperature:<sup>[7]</sup>

$$\varepsilon = \frac{\int_{\lambda_1}^{\lambda_2} (1 - R(\lambda))M_b(\lambda)d\lambda}{\int_{\lambda_1}^{\lambda_2} M_b(\lambda)d\lambda} \quad (\text{S13})$$

where  $R(\lambda)$  is the measured reflectance and  $M_b(\lambda)$  is the blackbody emissivity at room temperature. The wavelength  $\lambda$  is typically in the range of 2.5-25  $\mu\text{m}$ . In ASTM E1933, the wavelength range is considered from 2.5  $\mu\text{m}$  to 40  $\mu\text{m}$ . At a specific wavelength,  $\varepsilon$  can be calculated from the  $R(\lambda)$ .

$$\varepsilon(\lambda) = 1 - R(\lambda) \quad (\text{S14})$$

Therefore, the calculated emissivity spectrum for P4 is shown in Fig. S1f. The emissivity of P4 at 808 nm was determined as 0.97 ( $\varepsilon = 1 - 0.03$ ).

#### Characterization

Electrochemical studies were performed using a CHI624B (CH Instruments, Inc.) potentiostat with the PEDOT film as the working electrode (self-electrode), a platinum plate as the counter electrode, and a Ag/AgCl wire as the reference electrode; 0.1 M TBAPC/PC was the supporting electrolyte. The  $E_{1/2}=(E_{pa}+E_{pc})/2$  of the Fc/Fc<sup>+</sup> couple was 0.38 V against Ag/AgCl. The resistance ( $R$ ) of the conductive polymer films was measured using a potentiostat and a four-point probe (Macor probe, 1.00 mm probe spacing, 200  $\mu\text{m}$  tip radius, 100 g loads, Jandel, UK). The thickness ( $t$ ) of the conductive polymer films was measured using an Alpha step profilometer (Tencor Instruments, Alpha-step IQ) with an accuracy of 1 nm. The electrical conductivity ( $\sigma$ ) was calculated using the equation  $\sigma=ln2/\pi Rt$ . The charge carrier concentration, carrier mobility, and Hall coefficient were measured using an HMS-5300 Hall measurement system (Ecopia) with a magnetic field of 0.53 T at room temperature. Polymer films on PET films were cut to areas of  $1\times 1\text{ cm}^2$ , and the edge was soldered with In 95% Sn 5%. The polymer films were peeled off and weighed using a microbalance (Sartorius CPA2P, resolution of 0.001 mg). The heat capacity of the conductive polymer was measured using differential scanning calorimetry (DSC) 200 F3, Netzsch with a temperature range from  $-10\text{ }^\circ\text{C}$  to  $50\text{ }^\circ\text{C}$  at a heating rate of  $10\text{ }^\circ\text{C min}^{-1}$  under a nitrogen atmosphere. Particle size measurement was carried by dynamic light scattering (DLS) using Zetasizer nano ZS90 system (Malvern Instruments). DLS experiments showed that the solution of 40 wt% of Fe(Tos)<sub>3</sub> in *n*-butanol containing PEPG forms micelles of  $\sim 15\text{--}20\text{ nm}$  size that remain stable for 3 days (Figure S4). Upon the addition of the monomer, the solution underwent polymerization to yield strongly colored large particles ( $\sim 70\text{--}300\text{ nm}$ ) within 3 min, and then formed microscale particles within 1 h at  $25\text{ }^\circ\text{C}$ . At  $60\text{ }^\circ\text{C}$ , the polymerization occurred much faster than at  $25\text{ }^\circ\text{C}$ , affording microparticles within 5 min. The samples were exposed to an NIR laser ( $1.6\text{ W cm}^{-2}$ ) through an X-ray protective window at an angle of  $45^\circ$ . High resolution transmission electron microscopy (HR-TEM) was performed on a JEOL JEM-F200 at 120 kV. Grazing-incidence wide-angle X-ray scattering (GIWAXS) spectra were collected at the 3C beam line in the Pohang Accelerator Laboratory (PAL) using a monochromatized 10.25 eV ( $\lambda= 0.121\text{ nm}$ ) X-ray irradiation source with a two-dimensional charge-coupled device detector (Mar165 CCD). The scattering vector ( $q$ ) was calculated from the equation:  $q=4\pi\sin(\theta)/\lambda$ . The degree of crystallinity ( $\chi_c$ ) of the films was calculated using the following equation:

$$\chi_c = \frac{\sum A_{cr}}{\sum A_{cr} + \sum A_{am}} \quad (\text{S15})$$

where,  $\sum A_{cr}$  and  $\sum A_{am}$  are the summation of the integral area of the crystalline zone and amorphous zone, respectively.<sup>[8]</sup>



## Section 2. Supplementary tables

**Table S1. Preparation of PEDOT films with different conductivities and their electronic properties.**

Sample	Weight ratio	<sup>a</sup> Speed, rpm	<sup>b</sup> e-doping, V	<sup>c</sup> t, nm	<sup>d</sup> $\sigma$ , S cm <sup>-1</sup>	<sup>e</sup> p, cm <sup>-3</sup>	<sup>f</sup> $\mu$ , cm <sup>2</sup> V <sup>-1</sup> s <sup>-1</sup>	<sup>g</sup> S <sub>TE</sub> , $\mu$ V K <sup>-1</sup>	<sup>h</sup> PF <sub>TE</sub> , $\mu$ W K <sup>-2</sup> m <sup>-1</sup>
P1	<sup>j</sup> 1:10.5:5.3:0.31	1,500	0.9	185±3	1,320±60	(3.6±0.6)×10 <sup>23</sup>	0.023±0.01	65±3	570±50
P2	<sup>j</sup> 1:9.1:4.5:0.31	1,000	-	180±3	1,230±80	(2.5±0.2)×10 <sup>23</sup>	0.031±0.02	73±5	650±50
P3	<sup>j</sup> 1:10.5:5.3:0.31	1,500	0.5	184±3	1,140±110	(1.8±1.0)×10 <sup>23</sup>	0.040±0.01	78±4	700±60
P4	<sup>j</sup> 1:10.5:5.3:0.31	1,500	-	181±3	940±40	(1.1±0.7)×10 <sup>23</sup>	0.053±0.03	81±4	620±50
P5	<sup>j</sup> 1:9.1:4.5:0.31	1,000	0.1	180±3	920±70	(1.0±0.1)×10 <sup>23</sup>	0.058±0.03	110±6	1120±60
P6	<sup>j</sup> 1:10.5:5.3:0.31	1,500	-0.1	183±3	360±30	(2.9±0.5)×10 <sup>22</sup>	0.078±0.04	120±6	510±40
P7	<sup>k</sup> 1:3.1:6.2	1,000	-	180±3	300±10	(2.2±1.4)×10 <sup>22</sup>	0.085±0.06	28±1	23±1
P8	<sup>k</sup> 1:3.1:3.1	1,500	-	172±3	14±1	(5.0±3.8)×10 <sup>20</sup>	0.17±0.13	31±1	1.3±0.1
P9	<sup>k</sup> 1:3.1:0.4	2,500	-	180±3	0.247±0.02	(4.4±3.7)×10 <sup>18</sup>	0.35±0.13	50±2	0.061±0.005
P10	<sup>l</sup> 1:10.6:0.42	1,000	-	164±3	(4.7±0.3)×10 <sup>-2</sup>	(2.1±1.5)×10 <sup>18</sup>	0.14±0.10	-	-
P11	<sup>l</sup> 1:15.0:0.59	700	-	165±3	(8.2±0.6)×10 <sup>-3</sup>	(4.5±3.0)×10 <sup>17</sup>	0.11±0.08	-	-
P4d540	<sup>j</sup> 1:10.5:5.3:0.31	700	-	540±10	710±100	-	-	-	-
P4d1140		700	-	1,140±20	590±100	-	-	-	-
P4d1690		700	-	1,690±30	550±100	-	-	-	-
P4d2230		700	-	2,230±50	520±100	-	-	-	-

<sup>a</sup>Spin coating speed, <sup>b</sup>electrochemical applied constant potential vs. Ag/AgCl for doping or dedoping, <sup>c</sup>film thickness, <sup>d</sup>electrical conductivity, <sup>e</sup>carrier concentration, <sup>f</sup>Hall carrier mobility, <sup>g</sup>Seebeck coefficient and <sup>h</sup>power factor from thermoelectric effect, weight ratio of <sup>j</sup>EDOT: Fe(tos)<sub>3</sub>:PEPG:pyridine (40 wt% of Fe(Tos)<sub>3</sub> in n-butanol), <sup>k</sup>EDOT: FeCl<sub>3</sub>:PEPG (20 wt% of FeCl<sub>3</sub> in n-butanol), and <sup>l</sup>EDOT: Fe(Tos)<sub>3</sub>:pyridine

(36 wt% of  $\text{Fe}(\text{tos})_3$  in weight ratio of isopropyl alcohol:distilled water=0.7:0.3 solution). Composition: iron(III) *p*-toluenesulfonate ( $\text{Fe}(\text{Tos})_3$ ), poly(ethylene glycol)-block-poly(propylene glycol)-block-poly(ethylene glycol) (PEPG, average molecular weight 2,800).

**Table S2. The peak assignment and degree of crystallinity of various PEDOT films.**

Sample	Peak	Scattering vector, $\text{\AA}^{-1}$	d-spacing, nm	Relative area	$\chi_c$ , %
P1	(100)	0.49	1.29	48.2	51.5 $\pm$ 2.7
	(200)	0.99	0.63	3.3	
	Amorphous zone	1.95	0.32	48.5	
P2	(100)	0.45	1.34	31.8	39.9 $\pm$ 2.5
	(200)	0.94	0.67	8.1	
	Amorphous zone	2.02	0.31	60.1	
P3	(100)	0.51	1.24	30.1	37.3 $\pm$ 2.1
	(200)	1.03	0.61	7.2	
	Amorphous zone	2.05	0.31	62.7	
P4	(100)	0.47	1.33	33.7	38.0 $\pm$ 2.2
	(200)	0.89	0.71	4.4	
	Amorphous zone	1.72	0.37	62.0	
P5	(100)	0.44	1.38	58.3	61.5 $\pm$ 2.8
	(200)	0.93	0.67	3.2	
	Amorphous zone	2.04	0.30	38.5	
P7	(100)	0.47	1.34	7.2	10.9 $\pm$ 1.2
	(200)	0.97	0.65	3.7	
	Amorphous zone	2.10	0.30	89.1	
P8	(100)	0.48	1.31	5.4	7.4 $\pm$ 0.6
	(200)	0.97	0.64	1.9	
	Amorphous zone	2.06	0.31	92.6	
P9	(100)	0.50	1.26	0.5	1.2 $\pm$ 0.1
	(200)	0.99	0.63	0.7	
	Amorphous zone	2.07	0.30	98.8	
P10	(100)	0.51	1.23	1.7	1.7 $\pm$ 0.2
	(200)	0.96	0.66	-	
	Amorphous zone	2.06	0.30	98.3	
P11	(100)	0.54	1.17	0.2	0.2 $\pm$ 0.1
	(200)	-	-	-	
	Amorphous zone	2.07	0.30	99.8	

**Table S3. Film geometry and properties for simulation.**

Components	Property
Sample diameter	2.5 cm
PET thickness	100 $\mu\text{m}$
PEDOT thickness	180 nm
Heat capacity of PET	1,160 J/kgK
Absorption coefficient of PET	$10^4$ /m
Poisson's ratio of PET	0.5
Heat capacity of PEDOT	1,730 J/kgK
Density of PEDOT	1,830 kg/m <sup>3</sup>
Absorption coefficient of PEDOT	$2 \times 10^6$ /m
Young's modulus of PEDOT	$10^9$ Pa
Poisson's ratio of PEDOT	0.35
Emissivity of PEDOT	0.97
Heat transfer coefficient of air	10 W/m <sup>2</sup> K

**Table S4. The parameters for calculation of the photothermal conversion efficiency.**

Sample	$t$ , nm	$A_{808}$ , nm	$A_{1064}$ , nm	$\Delta T_{m,808}$ , K	$\Delta T_{m,1064}$ , K	$m_i C_{pi}$ , mJ K <sup>-1</sup>	$m_i C_{pi}/ha_{808}$ , s	$m_i C_{pi}/ha_{1064}$ , s	$ha_{808}$ , mW K <sup>-1</sup>	$ha_{1064}$ , mW K <sup>-1</sup>	$\eta_{PT,808}$ , %	$\eta_{PT,1064}$ , %
P1	185	0.478	0.676	86±2	75±2	0.74	1.24	1.82	0.59	0.39	40±1	17±1
P2	180	0.500	0.599	95±2	95±2	0.75	1.10	0.89	0.69	0.84	50±1	49±1
P3	180	0.511	0.622	102±2	86±2	0.77	1.21	0.88	0.63	0.84	49±1	43±1
P4	180	0.521	0.614	106±2	108±2	0.78	1.10	0.94	0.70	0.83	56±1	54±1
P5	180	0.500	0.599	99±2	100±2	0.76	1.12	0.93	0.68	0.82	52±1	50±1
P6	172	0.556	0.533	127±2	129±2	0.82	1.22	1.07	0.67	0.77	62±1	64±1
P7	175	0.468	0.597	117±2	107±2	0.80	1.04	0.94	0.76	0.83	71±1	54±1
P8	156	0.402	0.481	122±2	131±2	0.81	1.18	0.98	0.68	0.84	73±1	75±1
P9	151	0.357	0.380	127±2	143±2	0.82	1.25	1.02	0.65	0.83	78±1	93±1
P10	164	0.367	0.336	103±2	102±2	0.77	1.10	0.90	0.70	0.85	66±1	74±1
P11	165	0.409	0.405	98±2	106±2	0.76	1.11	0.91	0.69	0.85	58±1	68±1

$\Delta T_m$ : the maximum temperature difference of the film at 808 and 1064 nm,  $m_i C_{pi}$  is the mass of the system components times the heat capacity of system components (PET:  $3.7486 \times 10^{-3} \text{ T} + 0.04359 \text{ J g}^{-1} \text{ K}^{-1}$ , PEDOT:  $1.73 \text{ J g}^{-1} \text{ K}^{-1}$ ),  $ha$  is value of the heat transfer coefficient times the surface area of the system at 808 and 1064 nm,  $\eta_{PT}$ : photothermal conversion efficiency at 808 and 1064 nm, the laser power was 0.191 and 0.220 W for 808 and 1064 nm laser, respectively.

**Table S5. Comparison of the NIR sensitivities of photothermal photodetectors from the literature.**

Materials	T, K	Thickness, nm	Laser power, mW	$\lambda$ , nm	Bias, V	Voltage, $\mu$ V	Current, nA	Sensitivity	Ref.
Graphene	40	-	0.05	850	<sup>a</sup> -5, <sup>b</sup> 2, <sup>c</sup> 0	-	44.6	<sup>e</sup> $8 \times 10^{-4}$	[9]
Graphene	20	-	0.07	800	<sup>a</sup> 30, <sup>b</sup> 0	-	$5.0 \times 10^{-2}$	<sup>e</sup> $7 \times 10^{-7}$	[10]
Graphene	300	-	0.2	780	<sup>c</sup> 0	-	0.5	<sup>e</sup> $2.5 \times 10^{-6}$	[11]
Graphene	RT	-	5	1,550	<sup>d</sup> -15	-	$7.8 \times 10^3$	<sup>e</sup> $1.5 \times 10^{-3}$	[12]
					<sup>d</sup> 0	-	$5 \times 10^3$	<sup>e</sup> $1 \times 10^{-3}$	
					<sup>e</sup> 0.4	-	$4 \times 10^4$	<sup>e</sup> $6.1 \times 10^{-3}$	
Graphene	0.07	-	20	800	-	-	0.20	<sup>e</sup> $3 \times 10^{-6}$	[13]
Graphene	-	-	3	1,550	<sup>c</sup> 0	-	$4 \times 10^3$	<sup>e</sup> $5 \times 10^{-4}$	[14]
MoS <sub>2</sub>	RT	-	0.06	750	-	61	$2.3 \times 10^{-2}$	<sup>f</sup> 1	[15]
								<sup>e</sup> $3.8 \times 10^{-7}$	
poly[Cu <sub>x</sub> (C u-ett)]	RT		2.8	808	<sup>d</sup> 0	50	$8.2 \times 10^2$	<sup>f</sup> $1.79 \times 10^{-2}$	[16]
								<sup>e</sup> $2.93 \times 10^{-4}$	

PEDOS-C6	RT		163	808	No bias	910	$1.8 \times 10^4$	$^f 5.58 \times 10^{-3}$	[3]
								$^e 1.01 \times 10^{-4}$	
PEDOT (P5)	RT	180 nm			No bias	4.15	$1.12 \times 10^2$	$^f 2.07 \times 10^{-2}$	This work
								$^e 7.65 \times 10^{-4}$	
PEDOT (P3)	RT	180 nm			No bias	2.2	$2.4 \times 10^2$	$^f 1.08 \times 10^{-2}$	
								$^e 1.21 \times 10^{-3}$	

<sup>a</sup> $V_{BG}$ : back gate voltage, <sup>b</sup> $V_{TG}$ : top gate voltage, <sup>c</sup> $V_{SD}$ : source-drain voltage, <sup>d</sup> $V_G$ : gate voltage, <sup>e</sup>current sensitivity ( $A W^{-1}$ ), <sup>f</sup>voltage sensitivity ( $V W^{-1}$ )

**Table S6. Photothermoelectric voltage and power generation under solar light with various thickness samples.**

Sample	Additional setting	Device type	Solar Input, Sun	$V_{PTE}$ , mV	$\Delta T$ , K	$S_{PTE}$ , $\mu V K^{-1}$	$PF_{PTE}$ , $\mu W K^{-2} m^{-1}$	$I_{PTE}$ , $\mu A$	Power, nW	Surface power density, $mW m^{-2}$
P4	HC	STE1	1	0.54	6.9	78	580	20	11	$5.0 \times 10^{-2}$
P4d540	HC	STE1	1	1.12	15	77	420	48	53	$2.4 \times 10^{-1}$
	FL	STE2	2	6.26	63	99	690	200	1,240	5.7
P4d1140	HC, FL	STE2	2	7.07	75	95	630	220	1,590	7.2
	HC	STE1	1	1.26	17	75	330	56	70	$3.2 \times 10^{-1}$
	FL	STE2	2	6.32	67	95	530	210	1,350	6.2
P4d1690	HC, FL	STE2	2	7.26	81	90	480	250	1,790	8.1
	HC	STE1	1	1.32	18	74	300	67	89	$4.0 \times 10^{-1}$
	FL	STE2	2	6.37	68	94	480	240	1,520	6.9
P4d2230	HC, FL	STE2	2	7.5	85	89	430	280	2,110	9.6
	HC	STE1	1	1.37	19	73	280	77	110	$4.8 \times 10^{-1}$
	FL	STE2	2	6.12	65	94	460	260	1,580	7.2
P4d2230	HC, FL	STE2	2	7.25	82	89	410	310	2,220	$1.0 \times 10^1$
	FL, 4 legs, series	STE3	2	26.4	81	82	350	270	7,050	$3.2 \times 10^1$
	FL, 4 legs, parallel	STE4	2	7.19	81	89	410	1160	8,370	$3.8 \times 10^1$
Ref. 3	PEDOS-C6		-	0.90	8.7	103	360	3.3	2.9	$2.5 \times 10^{-2}$
Ref. 16	poly[Cu <sub>x</sub> (Cu-ett)]		-	0.050	-	-	-	0.82	0.041	-

HC: half-covered, FL: Fresnel lens = 2 Sun, One Sun ( $100 \text{ mW cm}^{-2}$  ( $=1,000 \text{ W m}^{-2}$ )), series: series connection between 4 legs, parallel: parallel connection between 4 legs, module: 54 legs series connection module device ( $2 \times 2.5 \text{ mm}^2$  each).

**Table S7. Comparison of the solar thermoelectric performance from the literature.**

Ref.	Solar absorber	TE material	Device environment	Light power condition	Area (cm <sup>2</sup> )	$\Delta T$ (K)	<sup>a</sup> $\eta_{TE}$ (%)	<sup>b</sup> Surface power density (mW m <sup>-2</sup> )	<sup>b</sup> Volume power density (mW m <sup>-3</sup> )	<sup>b</sup> Energy density (Wh g <sup>-1</sup> )
[17]	Black absorber	Bi <sub>2</sub> Te <sub>3</sub>	Vacuum, glass enclosure	299 Sun	~3.3	180	4.6	450	6.8 × 10 <sup>6</sup>	8.2 × 10 <sup>4</sup>
[18]	Selective absorber	n-type: (InGaAs) <sub>1-x</sub> (InAlAs) <sub>x</sub> p-type: (AgSbTe) <sub>x</sub> (PbSnTe) <sub>1-x</sub>	Solar concentrator, Fresnel lens	120 Sun	~225	~500	-	210	-	-
[19]	CNT	Bi <sub>2</sub> Te <sub>3</sub>	Ambient	980 nm laser (~1 Sun)	25	12	2.1	33,000	1.7 × 10 <sup>7</sup>	8.1
This work	None	P4d2230	Fresnel lens	2 Sun	2.2	81	0.025	38	2.1 × 10 <sup>8</sup>	420

<sup>a</sup>Thermoelectric efficiency based on ZT value.<sup>[15]</sup> For P4d2230, thermal conductivity (~0.37 W m<sup>-1</sup> K<sup>-1</sup>) and ZT=0.67 were used for the calculation. <sup>b</sup>Values are calculated from the dimension of an only thermoelectric material without the bulk solar absorber, glass encapsulation, solar concentrator, and vacuum chamber.

## Section 3. Supplementary Figures

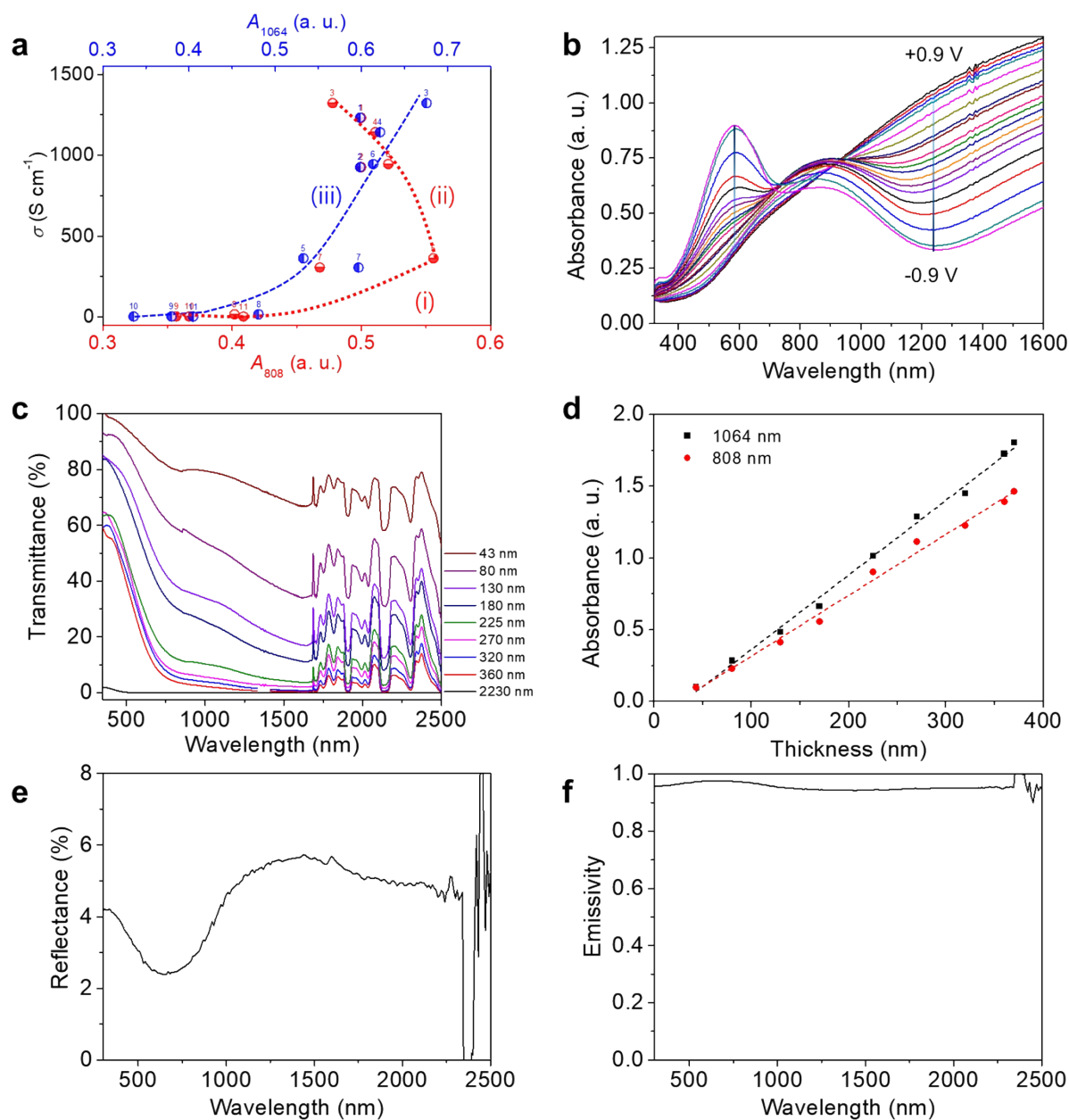


**Figure S1. UV-vis-NIR spectrum.** (a) Correlation of the absorbance at 808 and 1064 nm with conductivity of polymer film. (b) UV-vis-NIR spectra of 180-nm-thick P4 films with different oxidation levels. (c) UV-vis-NIR spectrum of pristine P4 film at different thickness (43–2230 nm) on PET substrate and (d) linear plot of absorbance at 808 and 1064 nm against film thickness. (e) The reflectance and (f) the emissivity spectrum of P4 (thickness: 180 nm).

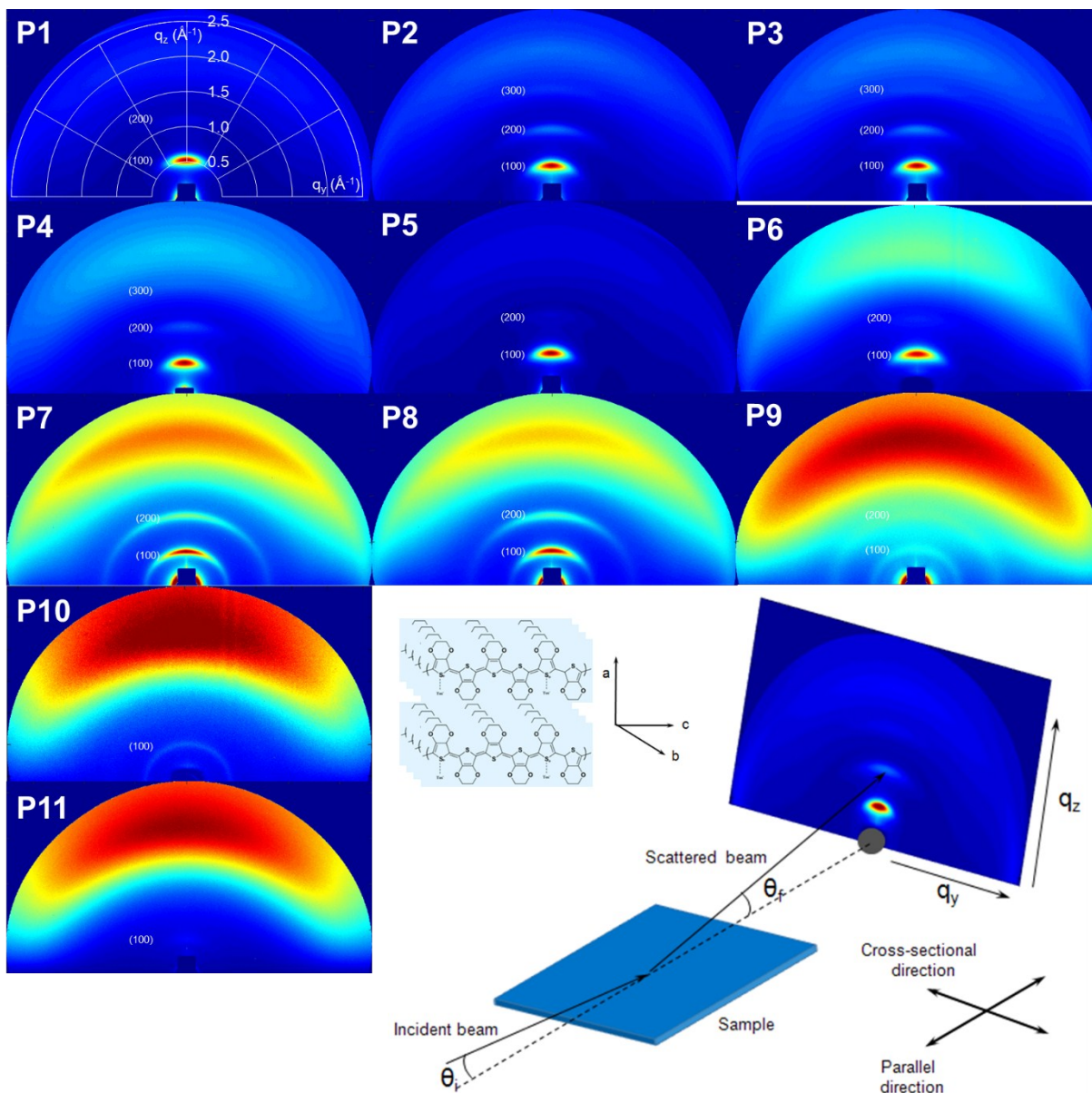


**Figure S2. Two-dimensional GIWAXS patterns for different PEDOT films.** GIWAXS spectra of P1–11 samples were measured at the critical angle of 0.10–0.13°. Schematic of the GIWAXS measurement.

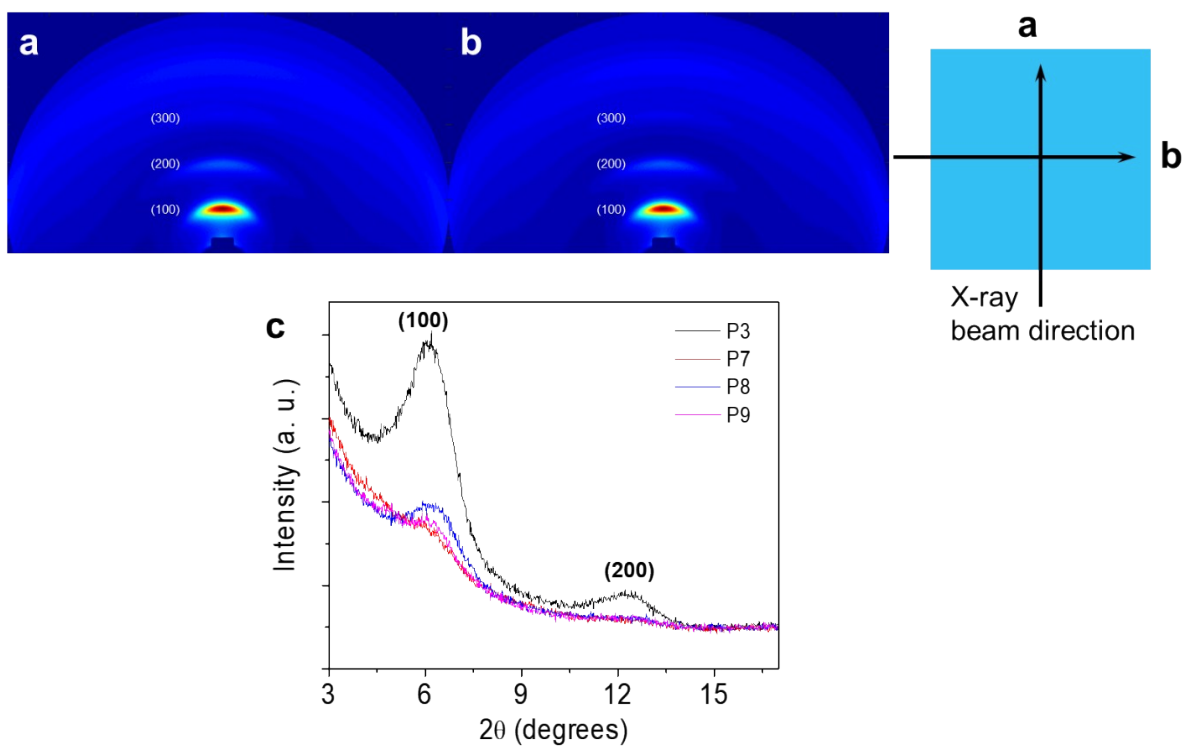


**Figure S3.** (a,b) Two-dimensional GIWAXS patterns for a P4 film with different X-ray beam directions in  $x$ - $y$  plane. (c) X-ray diffraction patterns of the PEDOT films with different conductivities.

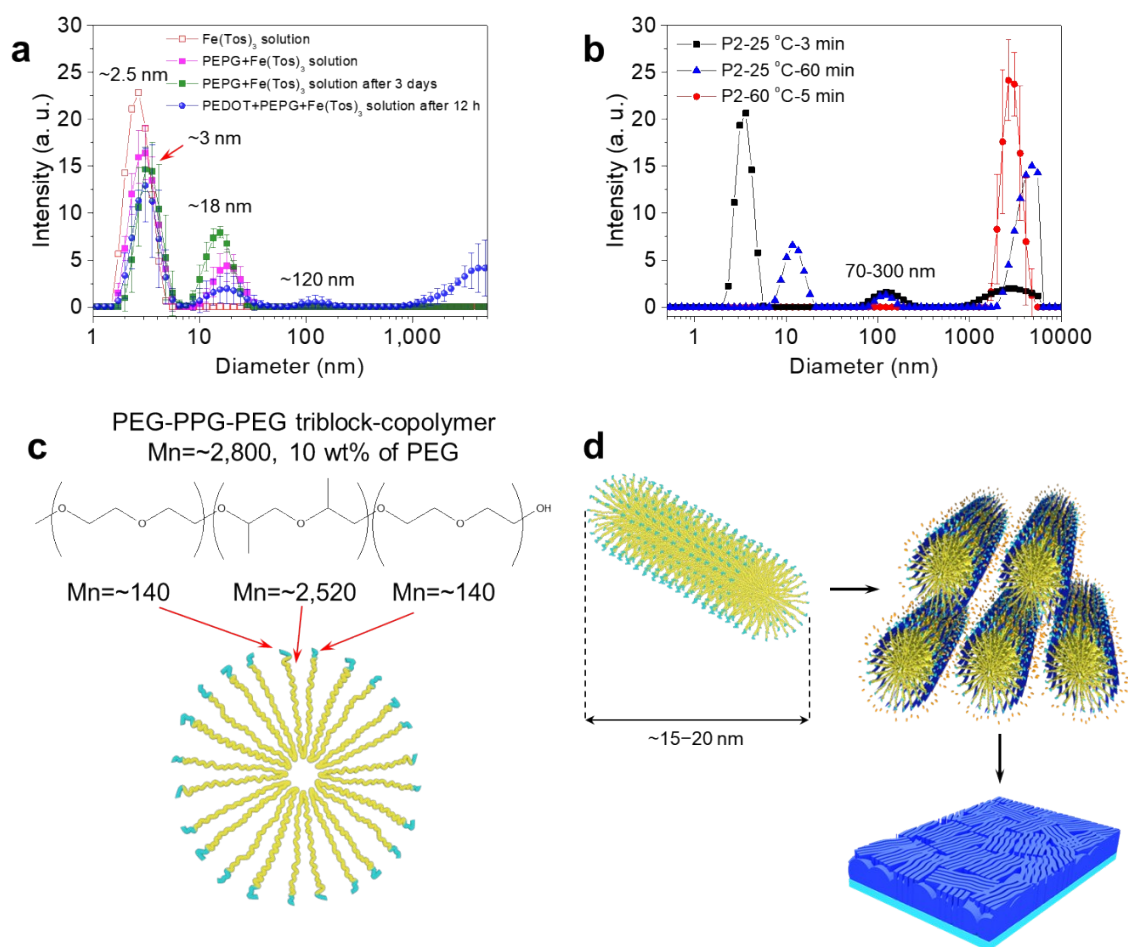


**Figure S4. DLS analysis.** (a,b) Size distribution data obtained from DLS measurement of the solutions. Schematics of (c) self-assembly of PEG-PPG-PEG triblock-copolymer and (d) micellar structures of PEPG, allowing the synthesis of highly crystalline PEDOT:Tos film.

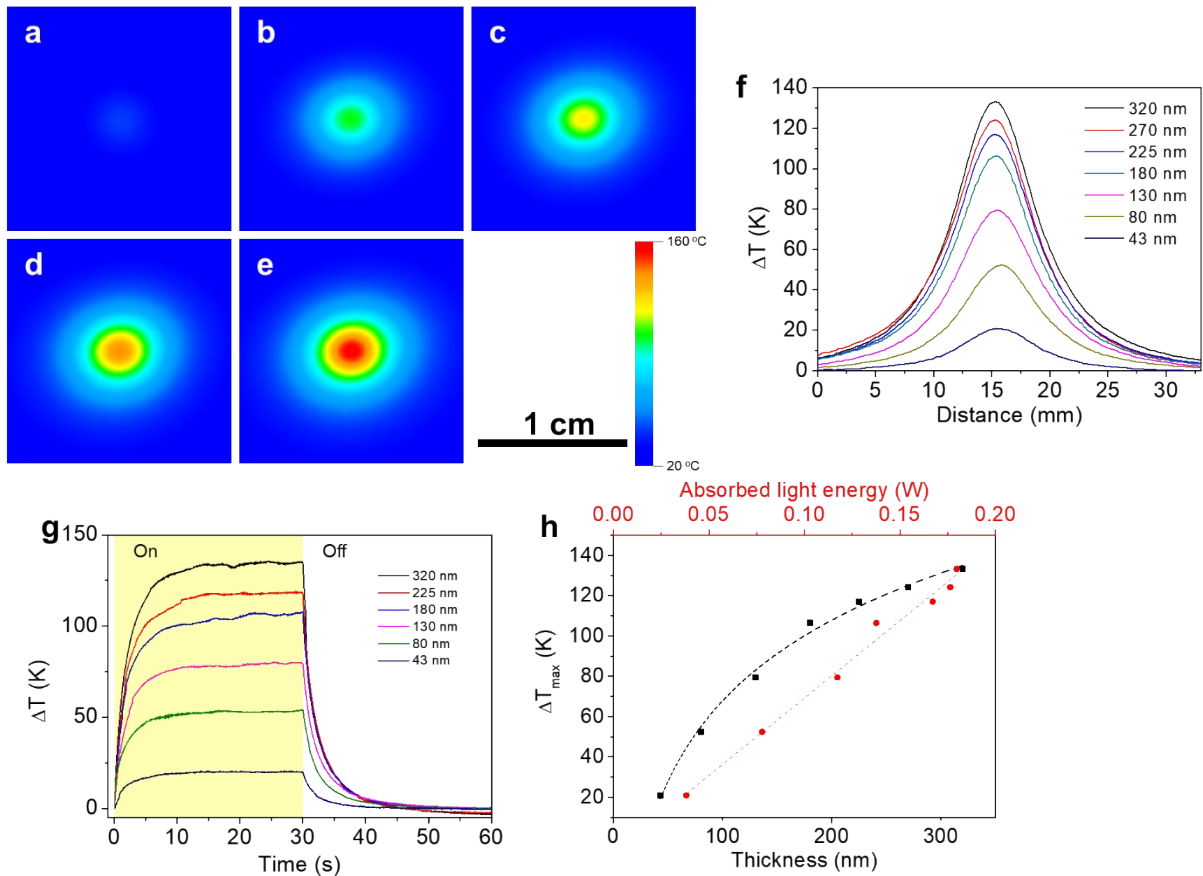


**Figure S5. Thermal images.** IR images of P4 films on PET substrates after irradiation with an 808-nm NIR laser (0.191 W) for 1 min with various film thicknesses of (a) 43, (b) 130, (c) 180, (d) 225, and (e) 320 nm. (f) The photothermally increased temperature distribution of different pristine P4 films on PET substrates using an 808-nm (0.191 W) laser. (g) Temperature increases of the P4 films of different thicknesses under NIR laser exposure (0.191 W). (h) The maximum temperature increases for P4 films with different thicknesses on PET substrates as functions of the thickness of the films and the absorbed light energy from the 808-nm (0.191 W) laser.

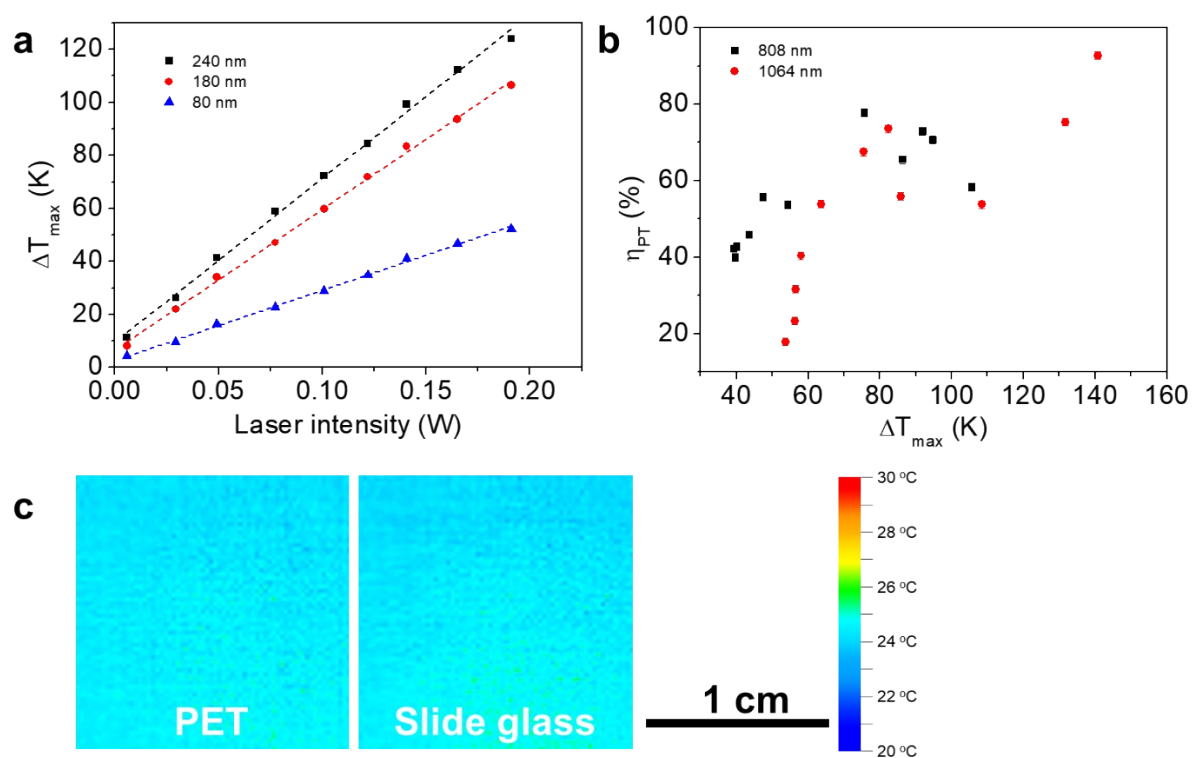


**Figure S6.** (a) Maximum temperature increases of P4 films on PET films with different thicknesses and irradiation with an 808-nm NIR laser. (b) Photothermal conversion efficiency of PEDOT with various polymerization conditions as a function of maximum temperature increase using 808-nm and 1064-nm lasers. (c) IR images of the substrates after irradiation with an 808-nm NIR laser (0.191 W) for 1 min.

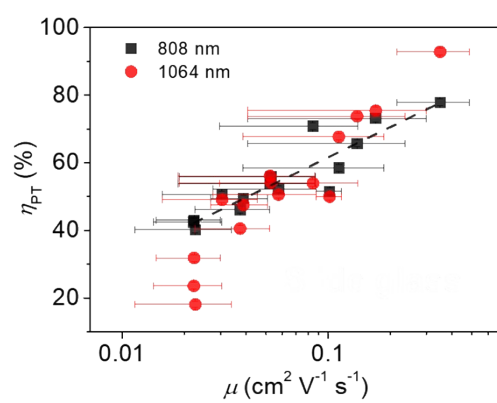


**Figure S7.** The photothermal conversion efficiency as a function of Hall carrier mobility.

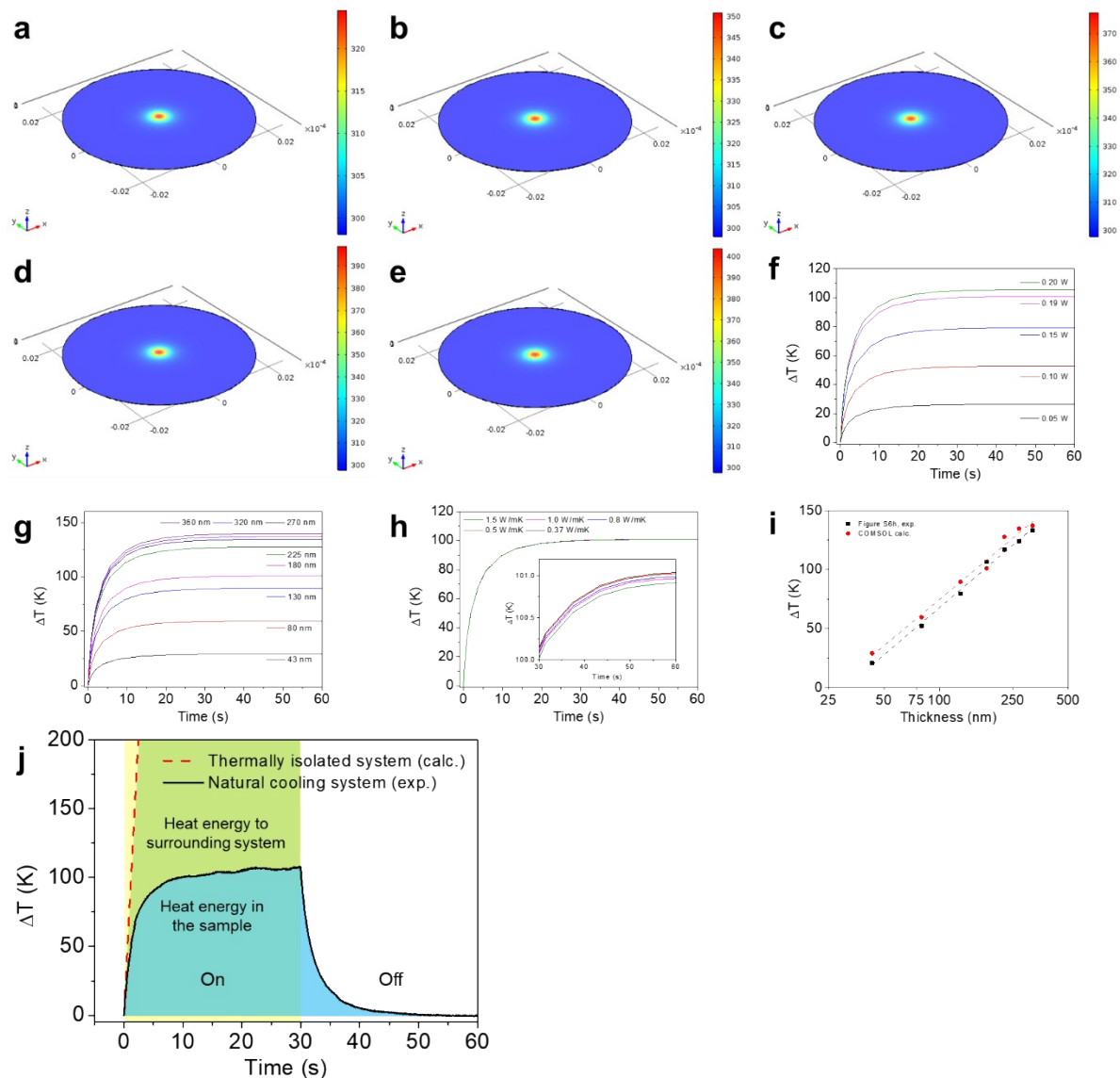


**Figure S8. Photothermal simulation.** COMSOL-simulated 3D temperature profile of the 180-nm-thick P4 film (thermal conductivity of  $0.37 \text{ W m}^{-1} \text{ K}^{-1}$ ) with various 808-nm laser powers of (a) 0.05, (b) 0.1, (c) 0.15, (d) 0.19, and (e) 0.2 W after 60 s. (f) Temperature increase over time for different laser powers, a-e. (g) Temperature increases over time for P4 films of different thicknesses of 43, 80, 130, 180, 225, 270, 320, and 360 nm after 60 s. (h) Temperature increase over time for various thermal conductivities of 0.37, 0.5, 0.8, 1.0, and 1.5 W after 60 s. (inset) Magnified region for 30–60 s. (i) Comparison of  $\Delta T_{\max}$  from Figure S5h and COMSOL simulation of the 180-nm-thick P4 film at 808-nm-laser power of 191 W. (j) Temperature increase of the 180-nm-thick P4 in calculation for thermally isolated system and natural cooling system from the 808-nm (0.191 W) laser.

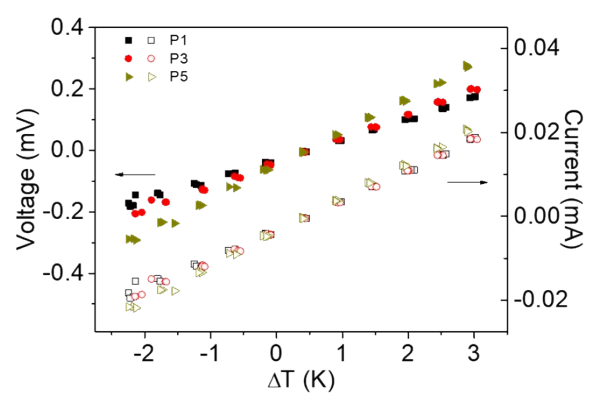


**Figure S9.** Seebeck voltage and current generation of PEDOT films with various conductivities.

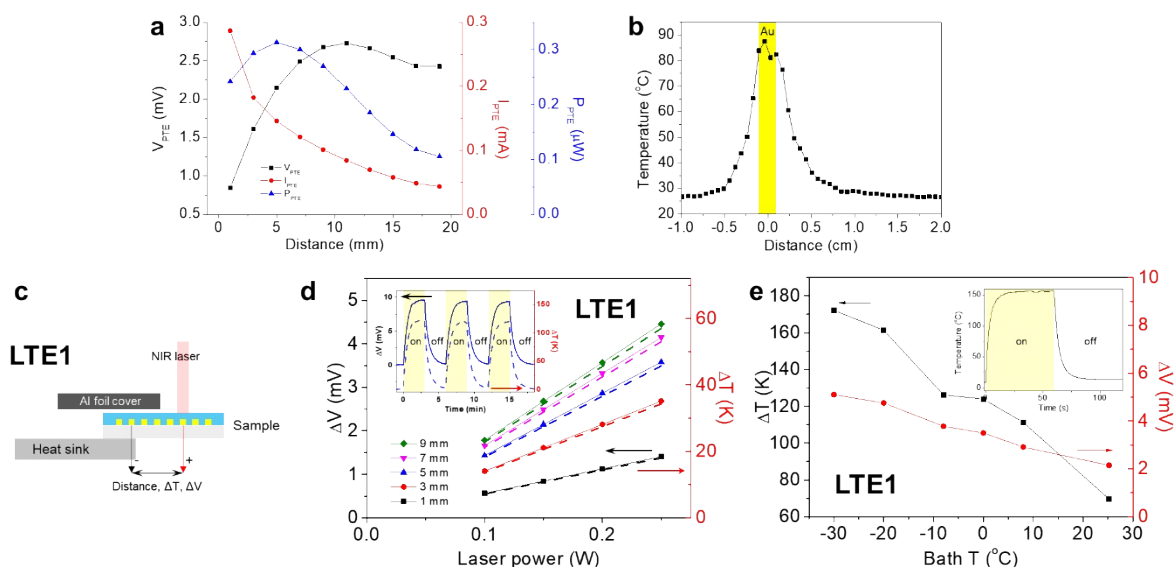


**Figure S10.** PTE voltage and current generation with different electrode distances under 808-nm laser irradiation (153 mW) of 180-nm-thick P4 films on PET under ambient conditions. (a) PTE voltage, current, and power generated under 808-nm laser with various electrode distances. (b) Temperature distribution with the distance of the electrode. (c-e) Photothermoelectric voltage and current generation under NIR laser. (c) Graphical image for one side cooled by a heat sink at different bath temperatures under 808-nm laser (LTE1). (d) Photothermal voltage and temperature generation of P4 with respect to laser power in measurement setting of LTE1 at room temperature. (inset) Temperature change under 0.15-W laser power at  $-30^{\circ}\text{C}$ . (e) Temperature change and photothermal voltage generation at various bath temperatures, at 0.15-W laser power. (inset) Temperature change at the bath temperature of  $-30^{\circ}\text{C}$ .

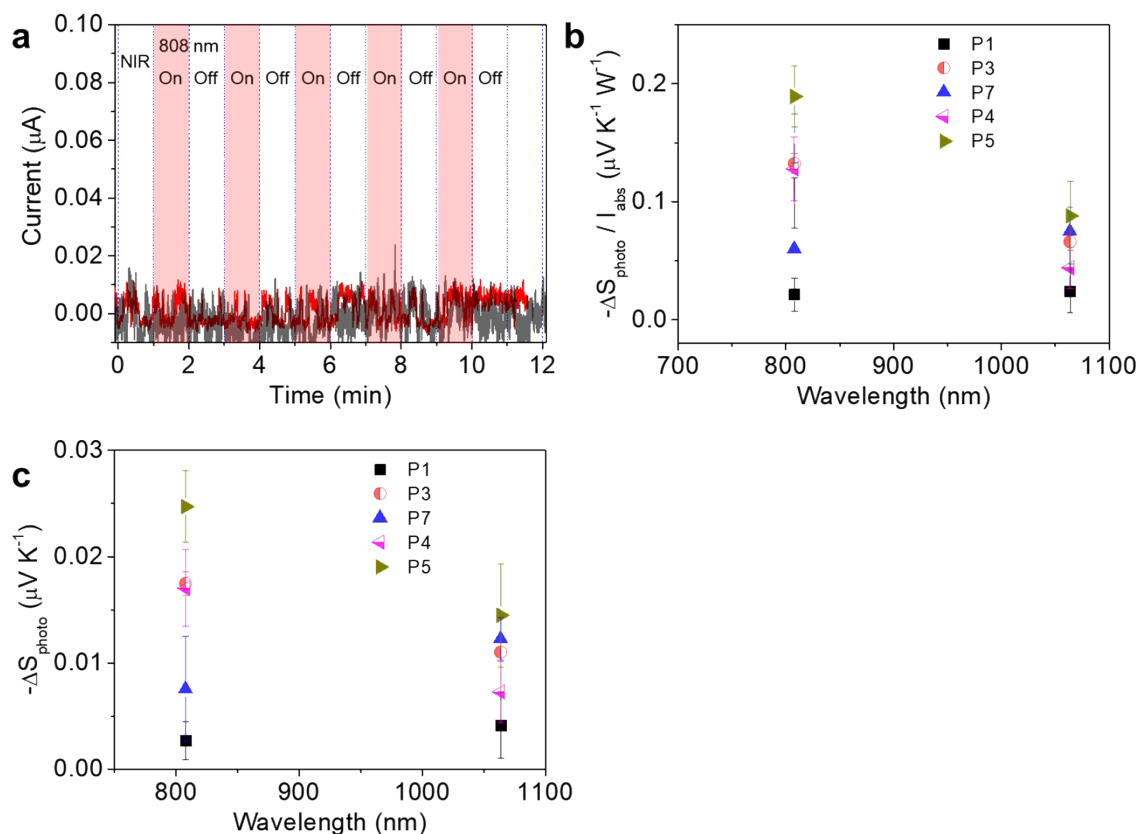


**Figure S11.** (a) Photothermoelectric voltage and current switching of an Au film on PET under different light sources in a vacuum chamber. (b) The changes in the photo-Seebeck coefficients per unit absorbed light power for P1, P3, P4, P5, and P7 films under different light wavelengths. (c) The changes in the photo-Seebeck coefficients for P1, P3, P4, P5, and P7 films under different light wavelengths. In the photo-Seebeck effect, the higher carrier concentration from the photoinduced excitation of PEDOT could result in electron–lattice coupling. Nevertheless, the  $-\Delta S_{\text{photo}}/I_{\text{abs}}$  is smaller than  $V_{\text{PTE}}/I$  because of the high carrier concentrations of intrinsic PEDOT films. Thus, the photo-Seebeck effect could be negligible in PEDOT films.

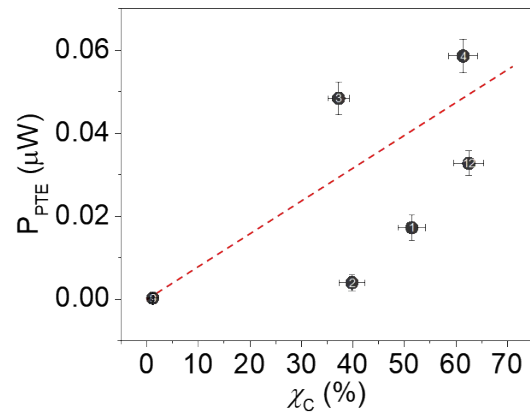


**Figure S12.** The correlation of the photothermoelectric power output and degree of crystallinity in PEDOT films.

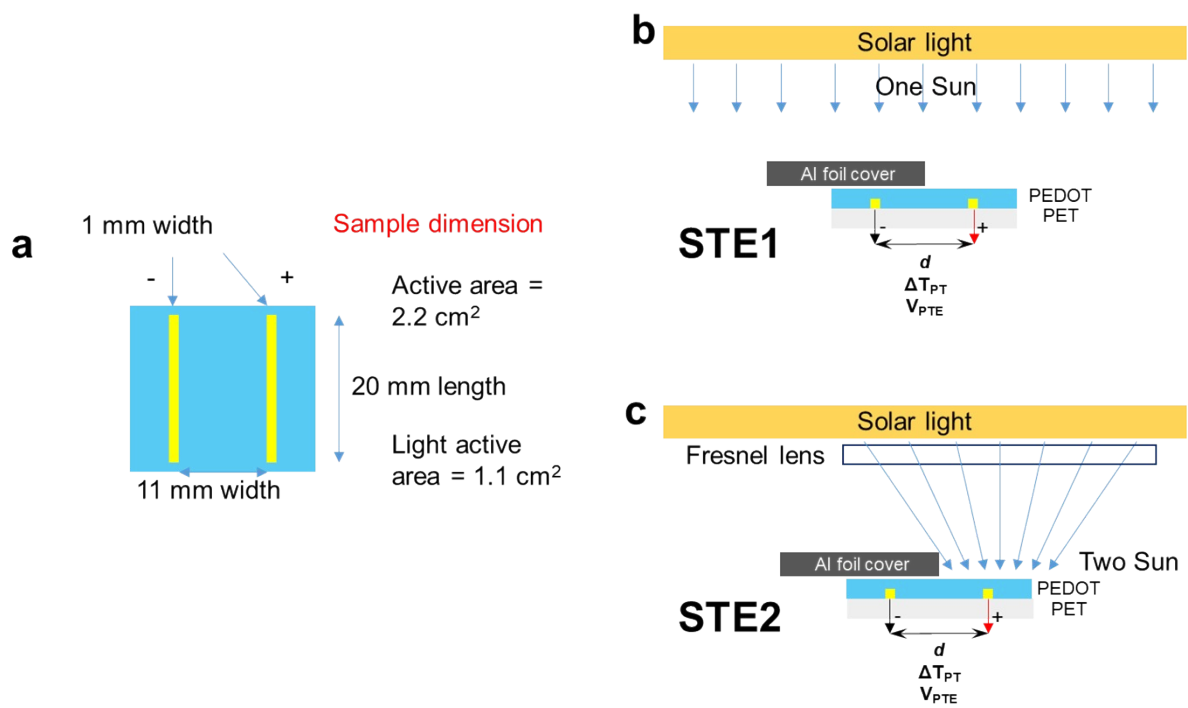


**Figure S13. Photothermoelectric device system under solar light.** (a) PTE device structure and dimension for horizontal type. (b) Half-covered sample by Al foil under one Sun. (c) One side of the sample is half covered by Al foil under two Sun using a Fresnel lens.

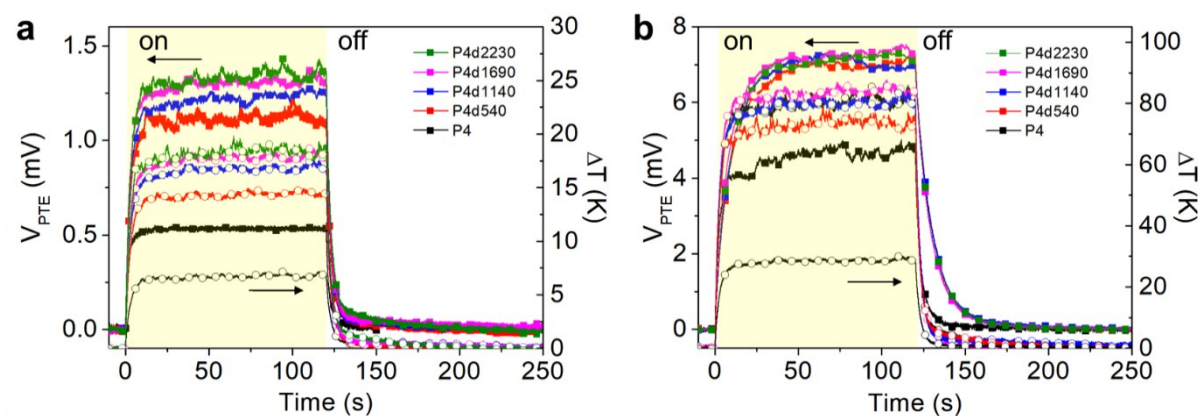


**Figure S14. Photothermoelectric voltage and temperature generation under solar light.** Photothermoelectric voltage and temperature rise under (a) one Sun irradiation and (b) two Sun irradiation by using Fresnel lens. One side of the samples was covered by Al foil. The other side of the samples was bare.

## Section 4. Supplementary references

- [1] L. Yan, M. Shao, H. Wang, D. Dudis, A. Urbas, B. Hu, *Adv. Mater.* **2011**, 23, 4120.
- [2] D. K. Roper, W. Ahn, M. Hoepfner, *The Journal of Physical Chemistry C* **2007**, 111, 3636.
- [3] B. Kim, H. Shin, T. Park, H. Lim, E. Kim, *Adv. Mater.* **2013**, 25, 5483.
- [4] Q. Tian, F. Jiang, R. Zou, Q. Liu, Z. Chen, M. Zhu, S. Yang, J. Wang, J. Wang, J. Hu, *ACS Nano* **2011**, 5, 9761.
- [5] A. Lösche, *Kristall und Technik* **1972**, 7, K55.
- [6] T. Park, J. Na, B. Kim, Y. Kim, H. Shin, E. Kim, *ACS Nano* **2015**, 9, 11830.
- [7] A. Bessiere, C. Marcel, M. Morcrette, and J-M. Tarascon, V. Lucas, B. Viana, N. Baffier, *J. Appl. Phys.*, **2002**, 91, 1589.
- [8] A. M. Hindeleh, D. J. Johnson, *Polymer* **1978**, 19, 27.
- [9] N. M. Gabor, J. C. W. Song, Q. Ma, N. L. Nair, T. Taychatanapat, K. Watanabe, T. Taniguchi, L. S. Levitov, P. Jarillo-Herrero, *Science* **2011**, 334, 648.
- [10] J. C. W. Song, M. S. Rudner, C. M. Marcus, L. S. Levitov, *Nano Lett.* **2011**, 11, 4688.
- [11] L. Pechtel, L. Song, D. Schuh, P. Ajayan, W. Wegscheider, A. W. Holleitner, *Nature Communications* **2012**, 3, 646.
- [12] T. Mueller, F. Xia, P. Avouris, *Nature Photonics* **2010**, 4, 297.
- [13] D. Sun, G. Aivazian, A. M. Jones, J. S. Ross, W. Yao, D. Cobden, X. Xu, *Nat Nano* **2012**, 7, 114.
- [14] F. Xia, T. Mueller, Y.-m. Lin, A. Valdes-Garcia, P. Avouris, *Nat Nano* **2009**, 4, 839.
- [15] M. Buscema, M. Barkelid, V. Zwiller, H. S. J. van der Zant, G. A. Steele, A. Castellanos-Gomez, *Nano Lett.* **2013**, 13, 358.
- [16] D. Huang, Y. Zou, F. Jiao, F. Zhang, Y. Zang, C.-a. Di, W. Xu, D. Zhu, *ACS Applied Materials & Interfaces* **2015**, 7, 8968.
- [17] D. Kraemer, B. Poudel, H.-P. Feng, J. C. Caylor, B. Yu, X. Yan, Y. Ma, X. Wang, D. Wang, A. Muto, K. McEnaney, M. Chiesa, Z. Ren, G. Chen, *Nat. Mater.* **2011**, 10, 532.
- [18] R. Amatya, R. J. Ram, *J. Electron. Mater.* **2010**, 39, 1735.
- [19] D. Xia, S. Jiang, C. Liu, S. Fan, L. Chen, *Sol. Energy Mater. Sol. Cells* **2015**, 141, 331.